NASA/ARMY/MIT ACTIVE TWIST ROTOR CLOSED-LOOP CONTROL TEST FOR VIBRATION REDUCTION

SangJoon Shin Carlos E. S. Cesnik
The University of Michigan
Ann Arbor, MI 48109, U.S.A.

Steven R. Hall
Massachusetts Institute of Technology
Cambridge, MA 02139, U.S.A.

Abstract

Closed-loop control experiments were conducted with the integrally twist-actuated helicopter rotor blades for reducing vibratory loads developed in forward flight. The rotor is a four-bladed fully articulated Active Twist Rotor (ATR) system. The integral twist deformation of the blades is obtained using Active Fiber Composite actuators embedded in the composite blade construction. The experiments were conducted at NASA Langley Transonic Dynamics Tunnel. During the test, rotor system response characteristics were first identified with respect to the blade twist actuation. Since a rotor in forward flight is a time-periodic system, the adopted methodology requires the determination of multi-component harmonic transfer functions. However, identification results indicate that the rotor system may be treated as a linear time-invariant system under the level flight conditions tested. The designed closed-loop controllers featured multi-harmonic and multi-mode characteristics. For the four-bladed ATR system, 4/rev is the primary target frequency for vibration reduction. There was also a significant 1/rev normal shear vibratory component (associated with blade tracking). The two cyclic modes were used to reduce the 4/rev vibration while the collective mode was employed for the 1/rev vibration. More than 40 dB of the hub normal shear vibratory load (lb) was eliminated at 4/rev. Another significant reduction was observed at 1/rev. Due to the open-loop characteristics of the ATR system, the other components of the fixed-system loads at 4/rev were in general reduced when minimizing the normal shear component. There were, however, increase in some of the higher frequency components of the vibration.

Nomenclature

C_T	non-dimensionalized rotor thrust coefficient
d	disturbance on the measurement
$\mathbf{D}^2$	second-order derivative operator matrix
$\mathbf{e}$	error vector
G	transfer function in Laplace domain
$\mathbf{G}$	harmonic transfer function estimate
G_i	harmonic transfer functions
J	cost function
n	number of data points in the input vector
n_h	number of harmonic transfer function
N	number of blades
t_d	actuation period
t_p	no actuation period between chirps
T	plant period
T_d	delay time
$\mathbf{T}$	control response matrix
$\mathbf{u}$	vector of N/rev actuation amplitudes
$U(j\omega)$	input matrix in frequency domain
$\mathbf{U}$	Fourier transformed input vector
$Y(j\omega)$	output matrix in frequency domain
$\mathbf{Y}$	Fourier transformed output vector
z	response of the plant vibratory load
$\mathbf{z}$	vector of vibration amplitudes
$\mathbf{z_o}$	vector of baseline vibration amplitudes
α	weighting scalar for $\mathbf{D}^2$
α_S	rotor shaft tilt angle
ϕ_{cl}	closed-loop response spectrum
ϕ_{ol}	open-loop response spectrum
$\mathbf{\Phi_{UU}}$	auto-correlation of $\mathbf{U}$
$\mathbf{\Phi_{UY}}$	cross-correlation of $\mathbf{U}$ and $\mathbf{Y}$
μ	advance ratio
ω_P	primary frequency of the plant
Ω	rotor rotational frequency
ψ	blade azimuth angle

Introduction

Higher harmonic control and individual blade control have been proposed as ways to reduce helicopter vibrations (Ref. 1, 2). These methods directly modify the excitation forces, principally aerodynamic forces acting on the rotor blades, to reduce or eliminate vibration. For a closed-loop control implementation coupled with these methods, the so-called **T** matrix approach is usually used to identify system transfer functions and determine the design of controllers (Ref. 1, 3, 4). More advanced control algorithms based on the basic **T** matrix

approach have also been developed and tested on an experimental rotor system in the wind tunnel (Ref. 1, 3, 4). Flight test on a modified OH-6A aircraft was also conducted successfully (Ref. 4). These controllers, in general, exhibited satisfactory performance in vibratory load reduction for either fixed or rotating-system loads. However, certain problems were identified that include excessive power requirement, limitations on actuator excitation frequency, and the extreme mechanical complexity required for hydraulic sliprings for IBC.

A variety of actuation mechanisms based on active materials have recently been suggested to overcome those problems shown in the conventional HHC (Ref. 5-7). By replacing the traditional hydraulic systems with active material-based actuators, potential advantages can be obtained in terms of weight, power consumption, and bandwidth. In the present study, an integral twist actuation concept is chosen among the various implementations (Ref. 8). Although each implementation results in different physical configuration, the closed-loop control may be developed from a common HHC scheme. A control algorithm based on the **T** matrix approach was implemented successfully on an active rotor blade with trailing edge flap driven by an X-Frame actuator in hover (Ref. 9). A similar scheme using optimal control theory was investigated analytically for possible application on a flap-actuated active rotor system (Ref. 10).

The NASA/Army/MIT Active Twist Rotor (ATR) program was conducted to investigate integral blade twist actuation for helicopter vibration reduction in a more comprehensive fashion. It is a collaborative research effort between the U.S. Army Research Laboratory, at NASA Langley Research Center, and the University of Michigan/MIT. Throughout this program, analysis and design methodologies were explored regarding an active blade with embedded actuators (Ref. 11). Using these methodologies, a prototype ATR blade was designed and fabricated for bench/hover tests (Ref. 12-13). After minor design modification, a set of active blades were manufactured and tested in forward flight (Ref.14-15). During the open-loop forward flight test, significant impact on both fixed- and rotating-system loads was observed from a prescribed blade twist actuation (Ref. 14-15). The success of the open-loop test motivated the development of an effective closed-loop controller for the ATR system.

For the successful design of a closed-loop controller, it is essential to understand in advance the transfer function relationship, for example, between the fixed-system loads and blade twist actuation. In the conventional **T** matrix approach, the characteristics of the system are determined only at the single frequency of interest by typically using open-loop sine-dwell test (Ref. 1, 3, 4). However, this approach neglects the importance of the system response at nearby frequencies, which may result in limited performance and potential instabilities of the closed-loop system.

Recently, transfer function relationships for different active rotors were identified experimentally over a wide range of frequencies using sine-sweep actuation (Ref. 9, 16). All these tests and the corresponding identification were conducted in hover. In forward flight, however, helicopters present a more complex behavior. While a helicopter rotor is a time-invariant system in hover, it becomes time-periodic in forward flight due to the periodicity from the aerodynamics environment. It is also known that the characteristics of a linear time-periodic (LTP) system can be completely described by multi-component harmonic transfer functions (Ref. 17, 18). Also, a practical system identification methodology was recently developed to estimate such multi-component harmonic transfer functions for a helicopter rotor in forward flight (Ref. 19).

This paper presents the closed-loop control studies for vibration reduction of the ATR system. It describes the methodology employed for system identification and the rotor characterization as LPT or LTI during forward flight. Continuous-time controllers are then designed based on modern control approaches. Multi-harmonic and multi-mode controller structures are implemented and tested in the ATR. Detailed discussion of the experimental results and corresponding conclusions are presented herein.

ATR characteristics

The original requirements for the ATR blade came from an existing passive blade used by NASA Langley. The baseline (passive) system had been well studied and characterized over the years, and is representative of a generic production helicopter (Ref. 20). The ATR blade was designed based on the external dimensions and aerodynamic properties of the existing baseline blade to be tested in heavy gas (R134a) medium. Table 1 summarizes the general blade dimension and shape characteristics.

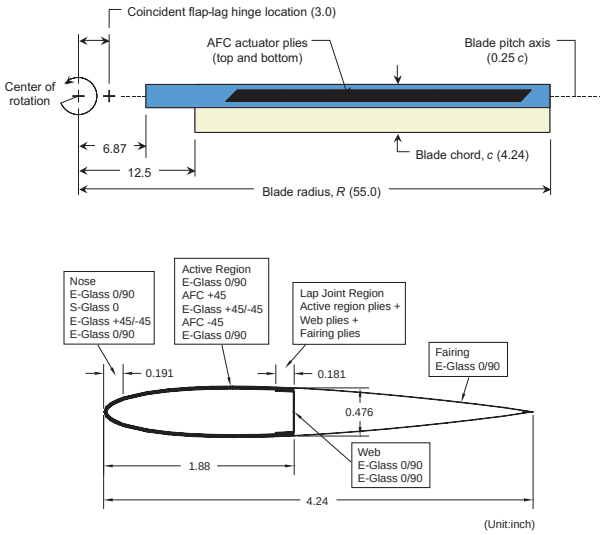

Figure 1. Planform and cross-section of the ATR prototype blade (Dimensions are in inches.)

The ATR blade employed a total of 24 Active Fiber Composite (AFC) packs placed on the front spar only, and distributed in 6 stations along the blade span (Ref. 17). Figure 1 shows basic blade planform and cross section characteristics selected for the ATR prototype blade. The front spar was further reinforced by one more 0/90° E-Glass ply added to the prototype blade design. Blade properties in Table 1 and the fan plot shown in Figure 2 are based on the final ATR design. The material properties of the passive prepregs and the AFC plies used in the blade are presented in the appendices of References 11 and 13.

Table 1. Characteristics of the ATR Blade

Description	Value
Rotor type	Fully articulated
Number of blades	4
Blade chord	10.77 cm
Blade radius	1.397 m
Solidity	0.0982
Section airfoil	NACA 0012
Blade pretwist	-10°
Hinge offset	7.62 cm
Root cutout	31.75 cm
Pitch axis	25% chord
Tension axis	34.4% chord
Center of gravity	17.9% chord
Lock number	9.0
Tip Mach number	0.6
Centrifugal loading at tip	738.5 g
Rotor speed	687.5 rpm
Rotor over speed	756 rpm
EA	$1.787\ 10^{1}$ N
GJ	$3.143\ 10^{1}$ N-m^2
EI_{flap}	$4.419\ 10^{1}$ N-m^2
EI_{lag}	$1.153\ 10^{3}$ N-m^2
Sectional torsional inertia	$3.810\ 10^{-4}$ kg-m
1st torsional natural frequency at 100% rpm	6.97/rev
Twist actuation at 0 rpm, 2,000 V_{pp}/0 V_{DC}	2.46°/m (peak-to-peak)

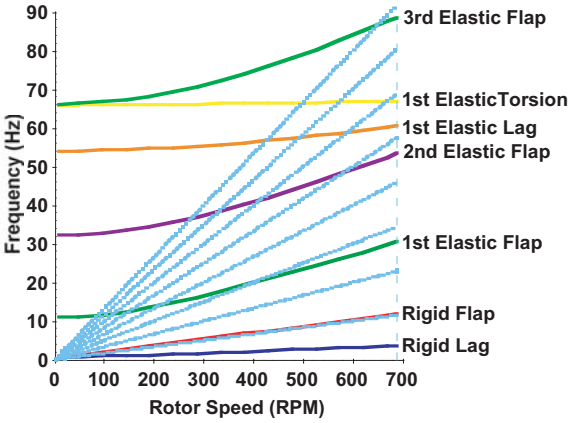

Figure 2. Fan plot of the ATR test blade

LTP system characteristics

In a linear, time-periodic system, a sinusoid input at single frequency ω generates a superposition of sinusoids at several frequencies of various amplitudes and phases. The multiple output frequencies are the input frequency modulated by the plant frequency ω_P, i.e., ω, $\omega+\omega_P$, $\omega-\omega_P$, $\omega+2\omega_P$, $\omega-2\omega_P$, … Although the number of frequencies to be superposed is theoretically infinite, they may be truncated for practical purposes, and the smallest number of them are retained, which adequately represents the system dynamics. Consider, for example, that only three frequencies in the output are to be accounted for. Then, the output Y comprises of the linear combination of the responses due to inputs at frequencies ω, $\omega+\omega_P$, and $\omega-\omega_P$. This is equivalent to considering the system output as a linear combination of three different harmonic transfer functions (each corresponding to one of the three frequencies): G_0, G_{+1}, G_{-1}, respectively. Thus,

$$Y(j\omega) = G_0(j\omega)\cdot U(j\omega) + G_{+1}(j\omega)\cdot U(j\omega - j\omega_p) + G_{-1}(j\omega)\cdot U(j\omega + j\omega_p) \quad (1)$$

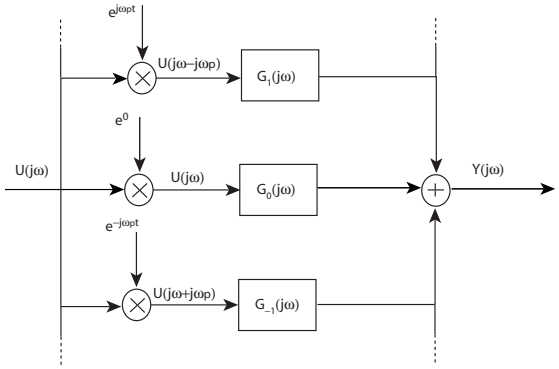

Figure 3. LTP system block diagram with three harmonic transfer functions

A linear system represented by Equation (1) is depicted in the block diagram in Figure 3.

However, since there is only one equation available in order to estimate three transfer functions G_0, G_{+1}, G_{-1}, the identification problem becomes underdetermined. This leads to the need for three different input applications, in order to obtain three independent equations, each of which is similar to Equation (1). Due to the periodic nature of the plant under consideration, it is important to account for the time of application of each input relative to the plant period T. In order for the plant behavior to be completely analyzed, multiple identical input signals are applied which are evenly distributed over the plant period. In Figure 4, an example of the input signals is shown. There, three input signals are created in sine-sweep (chirp) form with uniformly separated initiation interval T_d over the plant period T, where

$$T_d = T/3 = 2\pi/3\omega_p \tag{2}$$

Among the three input signals, the first one should have no delay between the start of the plant period and its initiation time. Then, the input U and output Y_0 can be modeled as in Figure 4. For the second signal, there should be a delay T_d seconds between them, and the input can be described as

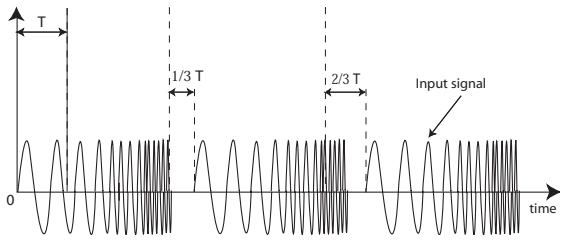

Figure 4. Input signal generated with appropriate time intervals over the plant period

$U(j\omega)e^{-j\omega T_d}$, which results in a block diagram shown in Figure 5. Similarly, the delay for the third signal is $2T_d$. Then, the vector of outputs Y can be expressed as

$$\begin{Bmatrix} Y_0 \\ Y_{1/3} \\ Y_{2/3} \end{Bmatrix} = \begin{bmatrix} U(j\omega) & U(j\omega - j\omega_p) & U(j\omega + j\omega_p) \\ U(j\omega) & U(j\omega - j\omega_p)W & U(j\omega + j\omega_p)W^{-1} \\ U(j\omega) & U(j\omega - j\omega_p)W^2 & U(j\omega + j\omega_p)W^{-2} \end{bmatrix} \cdot \begin{Bmatrix} G_0 \\ G_{+1} \\ G_{-1} \end{Bmatrix} \tag{3}$$

where $Y_{1/3}$ and $Y_{2/3}$ are the outputs due to the second and third chirp signals, respectively. Also, W is defined as $W = e^{j\omega_p T_d} = e^{j2\pi/3}$. Equation (3) can be written simply as

$$Y = U \cdot G \tag{4}$$

or to compute the harmonic transfer functions directly

$$G = U^{-1} \cdot Y \tag{5}$$

The derivation so far is based on the assumption that the output measurements due to each input signal must be conducted by allowing the response to settle down significantly before the next input signal is initiated. Then, it can be assumed that Y_0 is only due to the first input, $Y_{1/3}$ due to the second input, and so on. However, to make the identification process faster, input signals with less non-actuation time between successive signals are preferred. This leads to the idea of treating the entire input sequence as a single input signal, and similarly for the output signal. However, this will once more render the problem underdetermined. Further assumptions on

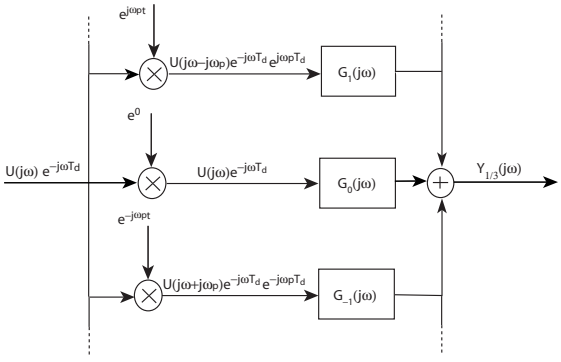

Figure 5. Delayed input signal and corresponding output of LTP system

the characteristics of G are required to make the problem well-defined. Therefore, a methodology to estimate harmonic transfer functions is adopted, which makes the problem constrained with these additional assumptions.

LTP system identification

The identification methodology developed in the previous section requires three sets of data, namely the input u, output y, and time measurements ψ (at which u and y occur). For rotor system identification, the information of ψ can be extracted from the record of the azimuth measurements. These data are recorded during the experiment in a discrete manner with some fixed sampling frequency. Therefore, all the data can be assembled in a vector of length n, where n is the total number of the data points. The input data can be expressed as

$$\begin{bmatrix} u_1 & u_2 & u_3 & \dots & u_n \end{bmatrix} \tag{6}$$

y and ψ are similarly defined. If n_h harmonic transfer functions of the system need to be identified, an $n_h \times n$ matrix $\mathbf{U}$ is constructed according to Equation (3) with an appropriately modulated and Fourier transformed vector $\mathbf{u}$ at each row, so that

$$\mathbf{U} = \begin{bmatrix} \mathbf{u}(\omega - m\omega_p) & \dots & \mathbf{u} & \dots & \mathbf{u}(\omega + m\omega_p) \end{bmatrix}^T \tag{7}$$

where $m = (n_h - 1)/2$. Similarly, $\mathbf{Y}$ can be constructed as the discrete Fourier transform of the vector y as

$$\mathbf{Y} = F\left\{\begin{bmatrix} y_1 & y_2 & y_3 & \dots & y_n \end{bmatrix}\right\} \tag{8}$$

Recalling that the empirical transfer function estimate of a linear time invariant (LTI) system involves the power and cross spectral densities of the input and output, these spectral densities can be defined in a similar manner for the LTP system as

$$\begin{aligned} \mathbf{\Phi}_{\mathbf{UU}} &= \mathbf{U}^* \mathbf{U} \\ \mathbf{\Phi}_{\mathbf{UY}} &= \mathbf{U}^* \mathbf{Y} \end{aligned} \tag{9}$$

where $\mathbf{U}^*$ is the complex conjugate of $\mathbf{U}$. Then, the transfer functions can be obtained for an LTP system similarly as in LTI case as

$$\mathbf{G}(\omega) = (\mathbf{\Phi}_{\mathbf{UU}})^{-1} \mathbf{\Phi}_{\mathbf{UY}} \tag{10}$$

where $\mathbf{G}(\omega)$ is the transfer function estimate with each harmonic transfer function G_i at its row as

$$\mathbf{G}(\omega) = \begin{bmatrix} G_{+m} & \dots & G_{+1} & G_0 & G_{-1} & \dots & G_{-m} \end{bmatrix}^T \tag{11}$$

Notice, however, that the computation of the transfer function based on Equation (10) will not yield an accurate result since only a few harmonics are considered instead of an infinite number. The cumulative effect of the neglected harmonics may be significant. Suppose that a given system has inherently N_h transfer functions of significant magnitudes, but only n_h of them are evaluated. Then, its output can be expressed as

$$\begin{aligned} \mathbf{Y} &= \sum_{k=-m}^{m} \mathbf{u}(\omega - k\omega_p) G_k + \mathbf{e} \\ &= \mathbf{U}^T \mathbf{G} + \mathbf{e} \end{aligned} \tag{12}$$

where the un-modeled part essentially appears as the error $\mathbf{e}$. In addition to this modeling error, the identification problem is still underdetermined. To solve this problem, an assumption is made that the transfer functions are relatively smooth, so it does not present drastic variations with frequency. This generates a minimization problem with a cost function J, which penalizes a quadratic error and the curvature of the transfer functions, so that

$$J = \min\left[\left(\mathbf{Y} - \mathbf{U}^T \mathbf{G}\right)^2 + \alpha\left(\mathbf{D}^2 \mathbf{G}\right)^2\right] \tag{13}$$

where $\mathbf{D}^2$ is a second-order differential operator, and α is a weighting factor. That is, the penalty term penalizes the curvature of the transfer function. Taking the derivative of J with respect to $\mathbf{G}$ in Equation (13) and setting it to zero, the minimizing $\mathbf{G}$ can be found as

$$\mathbf{G} = \left[\mathbf{U}^T \mathbf{U} + \alpha \mathbf{D}^4\right]^{-1} \mathbf{U}^T \mathbf{Y} \tag{14}$$

where $\mathbf{D}^4 = \mathbf{D}^2 \cdot \mathbf{D}^2$. Equation (14) is the final form that is utilized in the following system identification. Other issues on the practical implementation of Equation (14) and their solutions are provided in Reference 19.

Traditional HHC algorithm

Under the assumption of quasi-steady operation and linearity, the amplitudes of the sine and cosine components of the vibrations at the N/rev frequency can be formulated as

$$\mathbf{z} = \mathbf{z}_\mathbf{o} + \mathbf{T}\mathbf{u} \tag{15}$$

where $\mathbf{z}$ is a vector of vibration amplitudes (cosine and sine), $\mathbf{T}$ is the transfer matrix, $\mathbf{u}$ is the vector of the actuation amplitudes, and $\mathbf{z_o}$ is the vector of the vibration amplitudes with no actuation (baseline). In that equation, $\mathbf{z_o}$ is the disturbance to be rejected. The control algorithm traditionally adopted by previous

researchers (Ref. 1, 3, 4) is based on the idea of canceling the disturbance $\mathbf{z}_0$ by use of the higher harmonic swashplate input $\mathbf{u}$. Since the disturbance $\mathbf{z}_0$ is unknown, the approach is to measure the vibration at each time step and adjust the swashplate input $\mathbf{u}$ to just cancel that disturbance. The resulting control law is

$$\mathbf{u}_{n+1} = \mathbf{u}_n - \mathbf{T}^{-1}\mathbf{z}_n \tag{16}$$

where the subscripts denote the index of the time step. The measurement of the vibration $\mathbf{z}_n$ is accomplished by a Fourier decomposition of the vibration at the *N*/rev frequency, over the n-th time period. Hall and Wereley (Ref. 21) showed that the discrete- time system could be reduced to a simple LTI system when the helicopter dynamics are assumed to be linear and time-invariant (LTI), with transfer function *G(s)*. Then the control response matrix $\mathbf{T}$ is a 2×2 matrix and has the form

$$\mathbf{T} = \begin{bmatrix} a & b \\ -b & a \end{bmatrix} \tag{17}$$

where

$$a = \mathrm{Re}\{G(jN\Omega)\}, b = \mathrm{Im}\{G(jN\Omega)\}$$

With a slight simplification, the control law can be expressed in continuous time as shown in Figure 6. This control law is equivalent to an LTI compensator, *K(s)*, as given by

$$K(s) = \frac{2k(As + BN\Omega)}{s^2 + (N\Omega)^2}$$
$$k = 1/T$$
$$A = \mathrm{Re}\left\{\frac{1}{G(jN\Omega)}\right\} \tag{18}$$
$$B = -\mathrm{Im}\left\{\frac{1}{G(jN\Omega)}\right\}$$

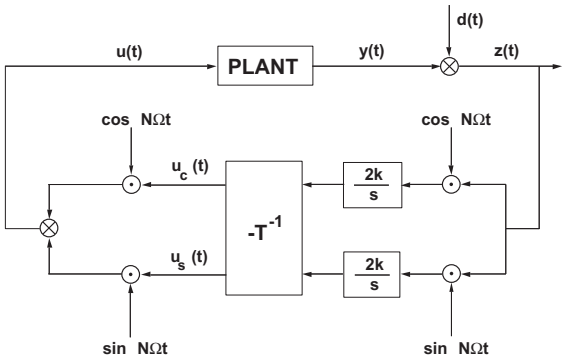

Figure 6. Block diagram of the higher harmonic control system adopted by other researchers (Ref. 1, 3, 4) using quasi-steady helicopter plant model

where *T* is the sampling period of discrete-time controller. Furthermore, this LTI feedback compensation structure turns out to be essentially the same as a classical disturbance rejection algorithm, which will eliminate a harmonic signal at constant frequency. Stability and performance issues of the closed-loop system associated with this feedback compensator are discussed in Reference 32. This analytical form enables the prediction of the stability of the closed-loop system before the controller implementation. Furthermore, this classical control formulation allows for control performance improvements by adjusting the control law to increase stability margins, increase overall gain, and so forth.

Experimental setup

The experiments for the system identification and closed-loop control of the ATR system were conducted at the Transonic Dynamics Tunnel (TDT) at NASA Langley Research Center. The Aeroelastic Rotor Experimental System (ARES) helicopter testbed was also used in the test. Detailed unique characteristics of the TDT and the ARES testbed are described in References 14 and 15. Figure 7 shows the ATR test blades mounted on the ARES helicopter

Figure 7. The ARES testbed inside the TDT with the ATR blades

testbed in the TDT. For this study, the active blade twist control algorithm was implemented in dSPACE (Ref. 22). That generates a prescribed input signal for system identification, and a control signal for the closed-loop control laws.

As described in the previous section, sinusoids are used to determine transfer functions, and more specifically, sine sweep waves (chirp signals) are used to obtain the system response over a specific range of frequencies. The chirps may have frequencies that vary linearly, quadratically, or logarithmically with time. The frequency content and time interval of the chirp is dependent on the system characteristics. It is also important to take into account the chirp phase in the case of an LTP system.

All the system identification tests were conducted in the heavy gas medium of the TDT at a nominal density of 2.432 kg/m^3. The rotor rotational speed throughout the test was held at 688 rpm, resulting in a nominal hover tip Mach number of 0.60. The rotor speed did vary slightly during the open-loop test. The small drifts in rotor speed were accounted for in the identification algorithms.

The flight conditions used in the tests are representative of helicopters in forward level flight (Table 2). For each flight condition, the rotor was trimmed to a nominal thrust coefficient C_T of 0.0066. The rotor was considered to be in trim when the first harmonic of blade flapping was less than 0.1° (Ref. 14, 15). This condition was referred to as "baseline." Data corresponding to the baseline condition was acquired first, and then the constructed chirp signal was applied to the ATR system. Data from the ARES testbed fixed-system balance, blade built-in strain gauges and accelerometer, and the high-voltage amplifier channels were recorded at a rate of 4,000 samples per second. Among them, the ARES 1P signal extracted from the rotor control system is composed of sharp peaks indicating the instant that Blade No. 1 passes through 0° azimuth location. This provides the azimuth information for the system identification. Due to a high sampling frequency and many channels of simultaneous acquisition used, data corresponding to each phase angle of chirp actuation had to be saved separately before proceeding to the next phase.

Table 2. Advance Ratios and Shaft Angle Pairs for the ATR Closed-loop Control Test (α_s is the shaft angle)

	μ = 0.140	μ = 0.200	μ = 0.267	μ = 0.333
α_s = -1°	X	X		
α_s = -2°			X	
α_s = -6°				X

For the closed-loop control tests, the flight conditions were the same as those tested for the system identification phase. The controllers used were all based on the transfer function identified at the highest advance ratio (μ = 0.333). Due to increased computer workload, the same basic set of data was recorded at 2,000 samples per second for the closed-loop control test. The controller targeted to suppress only the hub normal shear component. Thus, only the normal component from the rotor fixed-system balance is extracted and used as a reference signal **z(t)** for the closed-loop control. (See the definition of **z(t)** in Figure 6.) Unfortunately, at the beginning, an unidentified electrical problem caused this channel to be noisy. In particular, there were "spikes," or transients, in the signal, which induced the control system to produce control signals that were unrealistically large, and which did not reduce vibration. To eliminate this problem, a nonlinear filter was developed to remove these transients in real time.

System identification results

Before one can apply the system identification algorithm described in the previous section, the amplitude of the baseline loads must be subtracted from those under actuation. This is due to the definition of the transfer matrix that is used in the closed-loop controller design, as represented in Equation (15).

Since the load data under chirp actuation were saved separately for each phase division, these must be concatenated into a single array before the system identification algorithm is applied. In the test, 20-second duration was selected for t_d, the single actuation period, and 4-second for t_p, the non-actuation period between two successive actuation chirps, respectively. As a result, nine successive chirps (each with a different phase) generate an array approximately 200-s long. Furthermore, three sets of chirps were repeated for the same condition during the test, and used to estimate an average result on the harmonic transfer functions. Varying torques on the rotor system caused the rotor rotational speed to vary from its prescribed value (688 rpm), and were accounted properly during data reduction (Ref. 19).

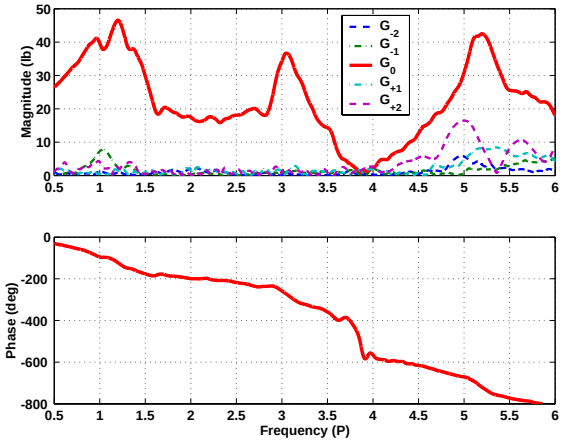

Figure 8. Harmonic transfer functions of the hub normal shear during the collective actuation for μ = 0.333, α_S = -6°, C_T = 0.0066, and 1,000 V twist actuation

As mentioned above, three different sets of data were acquired for each test condition. Also, after three data sets were acquired for the broad frequency range (5 to 70 Hz), the same condition was tested with a narrow frequency range of actuation. The narrow frequency range is used to obtain more accurate harmonic transfer function results near 4P. Thus, 40 and 52 Hz were selected for the lower and upper frequency bounds in the test, since 4P corresponds to 46 Hz in the case of the ATR system.

The system identification scheme developed in the previous section is applied to the concatenated input and output arrays with the weighting factor $\alpha = 10^{14}$ in Equation (14). Five harmonic transfer functions, G_{-2}, G_{-1}, G_0, G_{+1}, G_{+2}, are estimated simultaneously. Results for the hub normal shear are shown in Figure 8 for the case of collective blade actuation and flight condition μ = 0.333, α_S = -6°, C_T = 0.0066. The magnitudes of the five harmonic functions are shown in the figure; the phase is only shown for G_0. As can be seen in the figure, G_0 has an amplitude which is significantly larger than the others. Higher order components of the harmonic transfer functions appear to be negligible. This indicates that the response of the ATR system may be described only by the G_0 component, behaving like a linear time-invariant system, for the particular flight condition and blade actuation considered here. More insight about the blade dynamics can be also extracted from the G_0 result for the hub normal shear. It is observed that the peaks approximately match the frequencies of the rigid and elastic flap bending modes of the blade. (See the fan plot shown in Figure 2.)

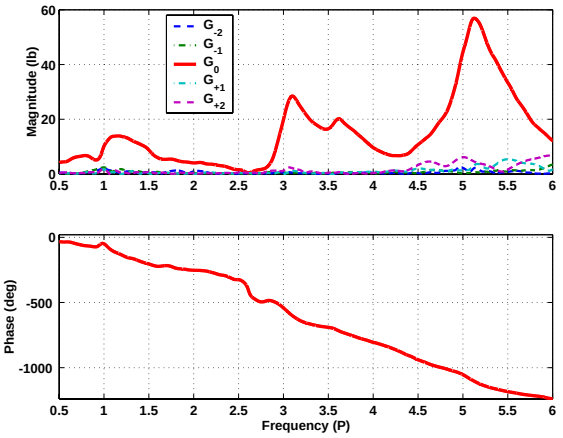

Figure 9. Harmonic transfer functions of the hub normal shear during the lateral cyclic actuation for μ = 0.333, α_S = -6°, C_T = 0.0066, and 1,000 V twist actuation

The harmonic transfer functions for cyclic actuation are shown in Figures 9 and 10. The results are similar to the results for collective actuation, in that the G_0 response dominates. Therefore, the ATR system may be considered as being LTI for cyclic actuation as well.

Notice also that the two cyclic modes of actuation exhibit much more control authority at 4P (approximately 10 lb for each mode) than the collective mode does (less than 2 lb). Thus, the two cyclic modes of blade actuation can be used more effectively to reduce 4P hub normal vibratory loads by the closed-loop controller for the level flight condition considered here. Ineffectiveness of the collective mode for 4P hub normal vibratory load

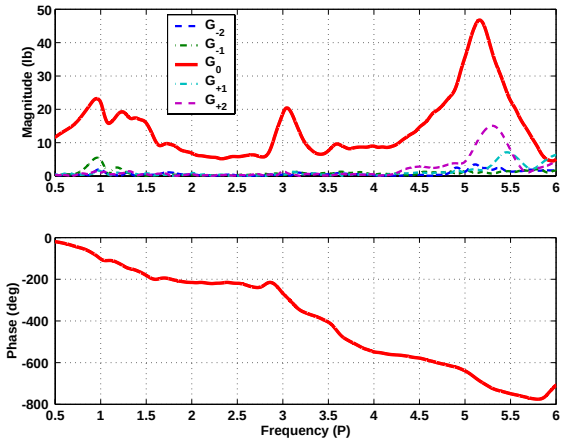

Figure 10. Harmonic transfer functions of the hub normal shear during the longitudinal cyclic actuation for μ = 0.333, α_S = -6°, C_T = 0.0066, and 1,000 V twist actuation

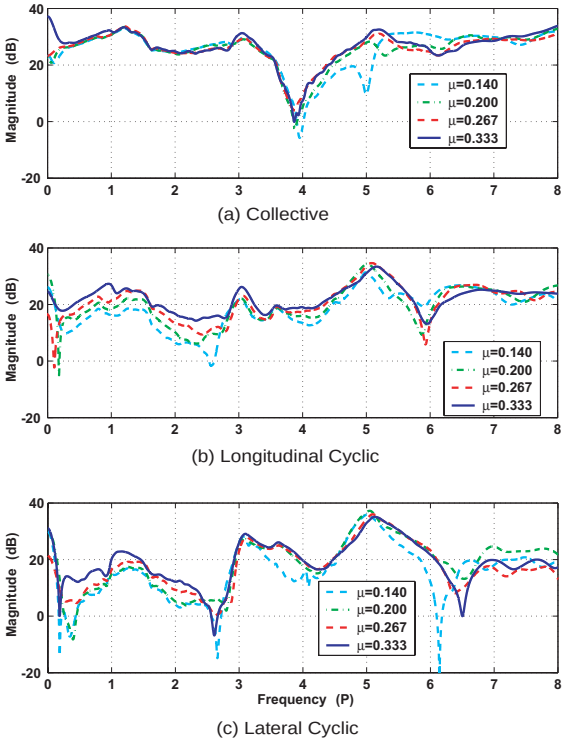

Figure 11. Transfer functions (magnitude only) of the hub normal shear during the three actuation modes for μ = 0.140, 0.200, 0.267, 0.333, and 1,000 V twist actuation

reduction was already observed in the ATR open-loop forward flight experiment (Ref. 21, 24). However, significant control authority is found at 1P frequency in the ATR system from the collective mode of actuation. This suggests the possible use of the collective mode for alleviating 1P vibratory loads, and therefore, improving blade tracking.

Transfer function results for the hub normal shear obtained for different flight conditions are shown in Figure 11. Again, the G_0 component shows much larger amplitude than the other higher-order harmonic transfer functions in each flight condition and blade actuation mode used. Thus, only the magnitude results of the fundamental transfer function, G_0, are provided for different advance ratios. It is observed that the transfer function varies slightly with advance ratio. This suggests the possibility of using a single control law for all 1-g flight conditions.

Controller structure

The actuation frequency and blade actuation mode used in the controller are selected based on the magnitude and phase of the corresponding transfer functions. Since the ATR is a 4-bladed rotor system, 4P is the primary frequency of hub shear vibratory loads. The ATR collective mode of blade actuation is relatively ineffective for affecting the hub normal shear. The longitudinal and lateral cyclic modes of actuation impart more significant influence on 4P hub normal shear. Therefore, these two modes of cyclic actuation are selected to suppress 4P vibratory loads of the hub normal shear. On the other hand, the collective mode shows a quite large control authority in 1P frequency component. Thus, the 1P collective mode is used to control the 1P vibration due to rotor tracking errors. This combination of different blade actuation modes at different frequencies results in a multi-harmonic and multi-mode structure for the controllers. The controllers are generated by combining multiple copies of the feedback structure of Figure 6 in parallel for each mode and frequency, as shown in Figure 12. This simple adaptation of the control architecture allows for many other harmonics of the vibration to be target for reduction. Prechtl and Hall (Ref. 21) have demonstrated this for a rotor in hover under the actuation of a flap.

The total control signal is the sum of the control signals from each single controller. However, the summation may force the resultant signal to exceed the voltage limit of individual actuators. Therefore, a device is needed to monitor the control signal and prevent saturation. To prevent the control input **u(t)** from exceeding the saturation limit, an anti-windup

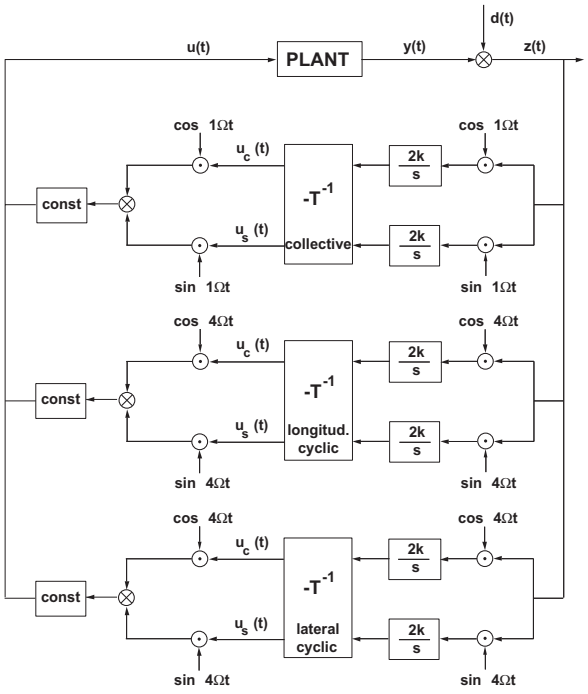

Figure 12. Block diagram of the multi-harmonic and multi-mode controller

mechanism is added to each feedback structure. Although it is not shown in Figure 12, this scheme constrains the control signal contribution from each feedback structure to a specific limit. The constant gain in front of each feedback structure, as shown in Figure 12, provides a way of assigning relative weight to the different modes of actuator. In the closed-loop experiment, many different combinations of these constant gains were attempted to determine the variation in vibration reduction performance from different controllers.

Closed-loop system stability

Before implementing the controllers, the stability of the closed-loop system should be examined. For this purpose, the loop gain, which is the product of the identified plant transfer function, $G_0(s)$, and the designed compensator, $K(s)$, is investigated in frequency domain. Since the plant transfer function was identified with respect to different blade actuation modes, examination of the closed-loop system stability is conducted for each mode. Among the actuation modes included in the controller (Figure 12), longitudinal cyclic mode at 4P is considered first. The Nichols plot for the closed-loop system without any modification on $K(s)$ is displayed as a dotted line in Figure 13 for the advance ratio condition μ=0.333. The stability of the system is ensured if there are no encirclements of the critical point (unity magnitude at 180° of phase). In the same plot, contours of constant disturbance attenuation (or amplification) are also plotted according to the relation

$$\frac{z}{d} = \frac{1}{\left(1 + G_0(s)K(s)\right)} \qquad (19)$$

The closed contours around the critical point with positive values represent degrees of vibration amplification. The thick, inverted U-shaped contour represents 0 dB boundary, where no vibration attenuation or amplification is obtained. The other contours indicate how much attenuation results (in dB) for the corresponding loop gain. Also, along the loop gain line, corresponding frequencies are designated with asterisks.

To aid in interpreting the level of vibration reduction or amplification, the magnitude of Equation (19) as a function of frequency is plotted in Figure 14. As expected, there exists a significant reduction of disturbance at the target frequency, 4P, in Figure 14. However, in the vicinity of 4P, there also appears an undesirable amplification of the disturbance. The amount of amplification present is related to the stability margin of the control system. From the

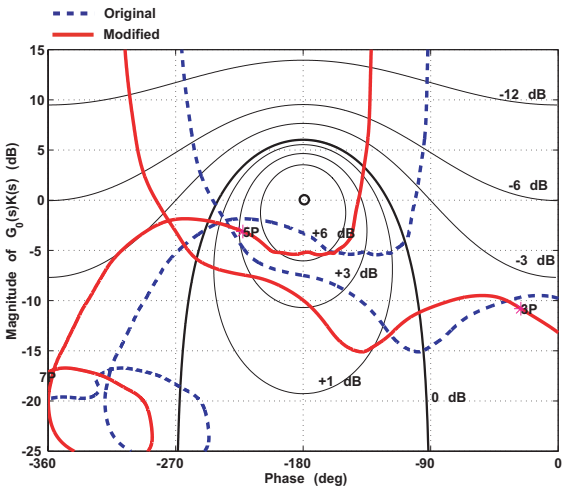

Figure 13. Nichols plot of the loop transfer function of the 4P longitudinal cyclic mode controller, original and modified, at μ=0.333

Nichols plot, the gain and phase margins are easily identified by measuring the proximity of the loop gain line to the critical point when the phase equals 180° or the gain equals unity, respectively. According to Figure 13, the present controller with the unmodified $K(s)$ turns out to have gain margin of approximately 3.2 dB, and phase margin of 70°. The low gain margin is the cause of the amplification of the vibratory load shown in Figure 14 near 3.7P and 5P. However, a modification to the original controller can improve performance. A simple solution is to alter the closed-loop phase characteristics, which is shifted by -40° at 4P from its original one. Such modification generates a new plot, which is shown as a solid line in Figure 13. Therefore, the controller

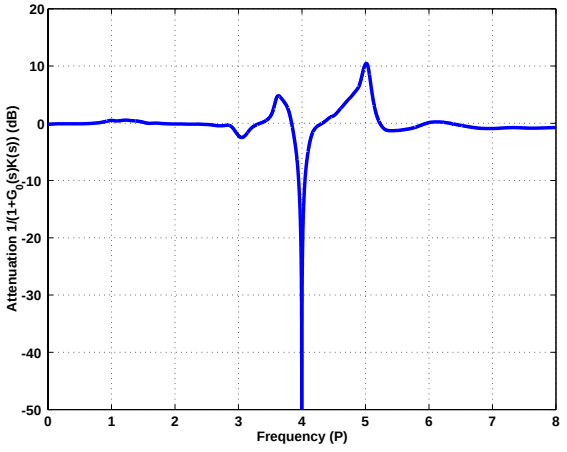

Figure 14. Attenuation of the ATR hub normal vibratory loads by engaging the closed-loop control through longitudinal cyclic mode actuation at μ=0.333

parameters A and B are modified by replacing $G(jN\Omega)$ in Equation (18) with a new one defined as

$$G(jN\Omega)\cdot e^{j(+40^\circ)} \qquad (20)$$

The other modes of blade actuation used in the controller, i.e., 4P lateral cyclic and 1P collective mode, are also modified in a similar way to the 4P longitudinal cyclic mode. The control signal from each controller is ultimately adjusted by an additional constant gain in front of each feedback structure before applied to the individual actuators, as shown in Figure 12.

Closed-loop control tests

As mentioned in the previous section, many different combinations of the blade actuation modes were examined in the closed-loop control test. In each combination, different gain constants were assigned to each feedback structure, and tested at different flight conditions. The combinations used in the test are summarized in Table 3. The closed-loop control test was conducted first at the high advance ratio flight condition, μ = 0.333, with the control parameters based on the system identification results from the same condition. In the very first case, only the 4P lateral cyclic mode was used for the controller, and then a combination of the two cyclic modes was used. In this two-cyclic-mode controller, the gain constants for each cyclic mode were increased from 0.5 to 1. At each increment of the gain constant, the total electric field generated by the controller and supplied to the individual actuators was monitored to make sure that it did not exceed the saturation limit. A gain constant of 1.0 is approximately the maximum that can be applied within the saturation limit in this two-cyclic-mode controller.

Next, the 1P collective mode is added to the two-cyclic-mode controller. From the transfer function results, relatively high control authority is observed at 1P for the collective actuation mode. Therefore, a small gain constant, 0.2, was assigned to 1P collective mode controller along with relatively larger constants for the other cyclic modes. In the three-mode controller, gain constants of (0.2, 1.0, 1.0) for collective, longitudinal cyclic, and lateral cyclic mode, respectively, give the maximum allowable electric field into the actuators. This three-mode controller with the parameters determined from the condition μ = 0.333 was also tested in other flight conditions (μ = 0.267, 0.200, 0.140). Since the gain combination of (0.2, 1.0, 1.0) generated approximately the maximum allowable electric field at μ = 0.333, only two combinations of gain constants, (0.2, 0.9, 0.9) and (0.2, 1.0, 1.0), were attempted in the other conditions.

Table 3. Assignment of Gain Constants for the Closed-loop Control Test

Case Name	1P Coll.	4P Long. Cyclic	4P Lateral Cyclic	Advance Ratio (μ)
Cyc1	0.0	0.0	1.0	0.333
Cyc2	0.0	0.5	0.5	0.333
Cyc3	0.0	0.707	0.707	0.333
Cyc4	0.0	0.9	0.9	0.333
Cyc5	0.0	1.0	1.0	0.333
CollCyc1	0.2	0.707	0.707	0.333
CollCyc2	0.2	0.9	0.9	0.333
CollCyc3	0.2	1.0	1.0	0.333
CollCyc4	0.2	0.9	0.9	0.267
CollCyc5	0.2	1.0	1.0	0.267
CollCyc6	0.2	0.9	0.9	0.200
CollCyc7	0.2	1.0	1.0	0.200
CollCyc8	0.2	0.9	0.9	0.140
CollCyc9	0.2	1.0	1.0	0.140

Control results

Since 4P is the primary frequency of interest for the ATR system, vibration reduction at 4P is computed and summarized in Table 4. Open-loop and closed-loop maximum 4P r.m.s. values are shown in the rightmost column and are referred to OL and CL rms (root-mean-square) normal load, respectively. As pointed out before, it is observed that there is a slight amplification of vibration around 4P when the controller is on. This amplification was predicted from the closed-loop system stability study (see Figure 13). Therefore, other estimates of vibration reduction are provided by integrating the response spectrum over a short interval across 4P frequency and comparing the open-loop and closed-loop cases. Four different integration intervals are considered here, such as 0.087P, 0.261P, 0.872P, as well as the whole spectrum. They correspond to 1 Hz, 3 Hz, 10 Hz, and the whole spectrum in Table 4, respectively. The vibration level, expressed in dB, is then formulated as

$$20\log_{10}\left[\frac{\sqrt{\int_{f_1}^{f_2}\phi_{cl}\,df}}{\sqrt{\int_{f_1}^{f_2}\phi_{ol}\,df}}\right] \qquad (21)$$

As shown in Table 4, the closed-loop controller based on the parameters determined at the high

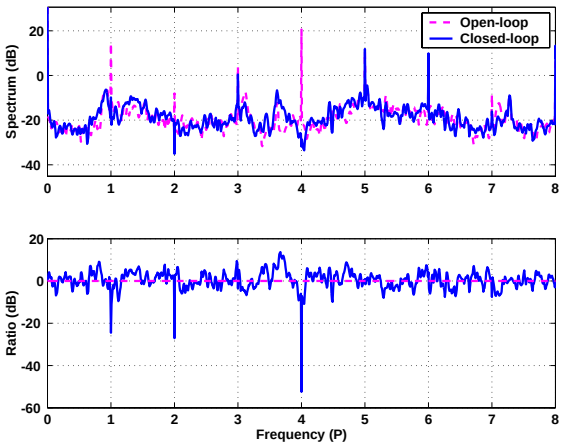

Figure 17. Open-loop and closed-loop spectra of the hub normal shear vibratory load in the case of CollCyc4

advance ratio, μ = 0.333, exhibits good vibration reduction performance at the different advance ratios. In fact, it shows even better performance at most of the other flight conditions than its designed one (μ = 0.333). This is because the open-loop (baseline) vibration level varies significantly among the flight conditions. (See the OL rms load column in Table 4.) One of the best reduction indices, approximately 40 dB, is obtained at μ = 0.267 with the gain combination (0.2, 0.9, 0.9), that is, Case CollCyc4. The corresponding spectrum is shown in Figures 17.

Frequency spectrum analysis of the control signal in the case of CollCyc4 reveals that it is composed of 1P and 3P sinusoidal signals, as shown in Figure 18. Because of the low control gain assigned at the 1P collective mode, the magnitude of the 1P component is relatively small. The large 3P component is a result of combination of the two cyclic modes applied at 4P. Their original frequency, 4P, is now changed into 3P due to the modulation with 1P to create the cyclic modes. It is also observed that each blade exhibits 90°. difference of its phase angle at 3P. This suggests that the 3P component of the generated control signal is close to the 3P IBC actuation signal used in the open-loop experiment. Note that the 3P IBC signals showed the biggest impact on the fixed-system load variation during the open-loop control test (Ref. 14).

The closed-loop controller used in the test was originally designed for attenuation of the ATR hub normal shear vibratory load only. However, it turns out that the other components among the fixed-system loads, such as longitudinal shear, lateral shear, pitching moment, and rolling moment, are reduced at the same time by the controller. Such simultaneous reduction of the fixed-system load component is similar to that observed in the ATR open-loop control test (Ref. 14). The closed-loop control signal generated to reduce the hub normal vibratory force results in a blade twist distribution that influences the other component in a similar way. The largest simultaneous reduction in the fixed-system loads is obtained in the case CollCyc4, which corresponds to the case where most reduction in the hub normal component is observed. Vibration reduction result for this case is shown in Figure 19.

Table 4. Vibration Reduction Results for the ATR 4P Hub Normal Shear

Case Name	Reduction Performance (dB)				OL rms normal load (lb)	CL rms normal load (lb)
	1 Hz	3 Hz	10 Hz	Spectrum		
Cyc1	-4.20	-4.20	-4.17	-0.009	22.35	13.77
Cyc2	-3.42	-3.42	-3.41	-0.013	22.45	15.14
Cyc3	-5.42	-5.42	-5.38	-0.051	22.52	12.06
Cyc4	-8.10	-8.09	-7.94	-0.027	22.55	8.87
Cyc5	-9.94	-9.94	-9.70	-0.042	22.61	7.19
CollCyc1	-5.35	-5.35	-5.29	-0.033	22.60	12.21
CollCyc2	-8.20	-8.19	-8.00	-0.048	22.50	8.75
CollCyc3	-9.33	-9.33	-9.15	-0.043	22.26	7.60
CollCyc4	-40.04	-30.10	-17.58	0.015	10.71	0.03
CollCyc5	-38.97	-30.53	-16.73	0.016	10.63	0.04
CollCyc6	-19.96	-19.83	-17.96	0.024	14.06	1.41
CollCyc7	-31.12	-29.51	-19.80	0.043	14.01	0.36
CollCyc8	-6.50	-6.50	-6.47	-0.004	21.45	10.15
CollCyc9	-7.77	-7.77	-7.71	0.012	21.35	8.72

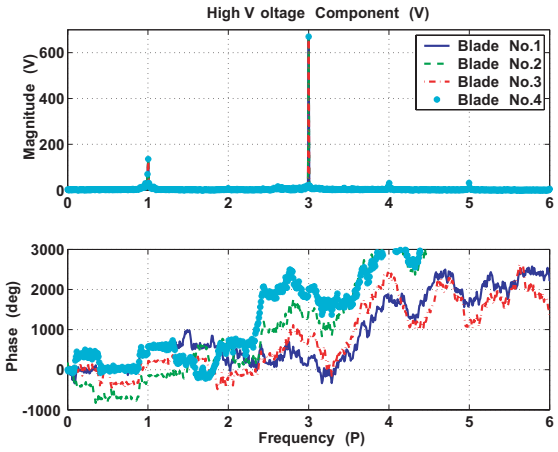

Figure 18. Frequency spectrum result of the generated blade control signal in CollCyc4

The vibration levels for all six components are significantly reduced, except for the yaw component, which is almost unaffected. Although a multi-component controller is expected to exhibit better performance, its design and implementation were not attempted in this study.

Conclusions

In this paper, the system identification and closed-loop control tests of the ATR system were described. The primary goal of this study was to demonstrate closed-loop control for the reduction of vibratory loads induced in forward flight, and it was successfully achieved. The system identification approach employed herein can determine the importance of periodicity for closed-loop control. For the ATR rotor, the periodic effects were shown to be unimportant, and, therefore, the system can be treated as linear and time-invariant. The system identification reveals that cyclic twist control is much more effective than collective twist control in reducing 4P vibration in the ATR rotor. It was also found that the transfer functions of the rotor do not significantly vary with level flight conditions, so that a single control law can be used to effectively control vibration over a wide range of advance ratios.

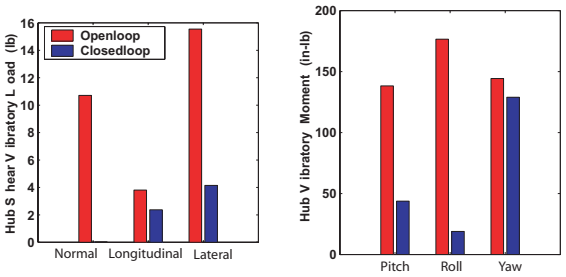

Figure 19. Reduction of the fixed-system loads at 4P in the case of CollCyc4

For the closed-loop control tests, a continuous-time control law was used, which is basically the T matrix approach recast as a continuous-time formulation. In this form, the control law is fundamentally the same as classical disturbance rejection control laws. Classical control techniques can be used to evaluate the efficacy of the control law, and to modify it to improve performance. For this narrowband disturbance rejection problem, the Nichols plot is a particularly effective design tool. Both 1P and 4P vibrations were simultaneously controlled by using collective twist actuation for the 1P component and a combination of longitudinal and lateral cyclic actuations for the 4P component.

Closed-loop tests of the ATR rotor produced significant levels of vibration reduction in all tested advance ratios. In some flight conditions, the 4P vibration was practically eliminated (40 dB reduction). It was also found that controlling the 4P and 1P vibrations indirectly reduced the vibration level of other harmonics, although by a lesser amount. The controller implemented in this work addressed vibration at two frequencies (1P and 4P) using three modes of actuation (collective twist, and two cyclic twists). It can, however, be easily extended to control other harmonics of the vibration as well.

Acknowledgements

The authors are especially thankful to Messrs. Matthew L. Wilbur, William T. Yeager, and Chester W. Langston (U.S. Army Vehicle Technology Directorate, NASA Langley Research Center) for their support in conducting the wind tunnel tests, and to Dr. Kyungyeol Song (Department of Aeronautics and Astronautics, Massachusetts Institute of Technology) for providing help on the system identification methodology. This work was sponsored by NASA Langley Research Center under the cooperative agreement number NCC1-323, and also supported by the U.S. Army Research Laboratory and the U.S. Army Research Office under contract number DAAD19-01-1-0390.

References

1. Shaw, J., Albion N., Hanker E. J., and Teal, R. S., “Higher Harmonic Control: Wind Tunnel Demonstration of Fully Effective Vibratory Hub Force Suppression,” Journal of the American Helicopter Society, Vol.31, (1), 1989, pp. 14-25.

2. Ham, N. D., "Helicopter Individual-Blade-Control Research at MIT 1977-1985," Vertica, Vol.11, (1/2), 1987, pp. 109-122.

3. Molusis, J. A., Hammond, C. E., and Cline, J. H., "A Unified Approach to the Optimal Design of Adaptive and Gain Scheduled Controllers to Achieve Minimum Helicopter Rotor Vibration," Journal of the American Helicopter Society, Vol.28, (2), 1983, pp. 9-18.

4. Wood, E. R., Powers, R. W., Cline, J. H., and Hammond, C. E., "On Developing and Flight Testing a Higher Harmonic Control System," Journal of the American Helicopter Society, Vol.30, (1), 1985, pp. 3-20.

5. Loewy, R., "Recent Developments in Smart Structures with Aeronautical Applications," Smart Materials and Structures, Vol. 6, 1997, pp. 11-42.

6. Friedmann, P. P., "The Promise of Adaptive Materials for Alleviating Aeroelastic Problems and Some Concerns," Innovation in Rotorcraft Technology, London, United Kingdom, June 24-25 1997.

7. Chopra, I., "Status of Application of Smart Structures Technologies to Rotorcraft Systems," Journal of the American Helicopter Society, Vol.45, (4), 2000, pp. 228-252.

8. Giurgiutiu, V., "Recent Advances in Smart Material Rotor Control Actuation," AIAA/ASME/ASCE/ AHS/ASC 41st Structures, Structural Dynamics and Materials Conference, AIAA Paper No. 2000-1709, Atlanta, GA, April 2000.

9. Prechtl, E. F., and Hall, S. R., "Design and Implementation of a Piezoelectric Servo-Flap Actuation System for Helicopter Rotor Individual Blade Control," AMSL Report #00-03, Active Materials and Structures Laboratory, Massachusetts Institute of Technology, January 2000.

10. Depailler, G., and Friedmann, P. P., "Reduction of Vibrations due to Dynamic Stall in Helicopters using an Actively Controlled Flaps," AIAA/ASME/ASCE/ AHS/ASC 43rd Structures, Structural Dynamics and Materials Conference, AIAA Paper No. 2002-1431, Denver, CO, April 2002.

11. Cesnik, C. E. S., and Shin, S. J., "On the Modeling of Integrally Actuated Helicopter Blades," International Journal of Solids and Structures, Vol.38, (10-13), 2001, pp. 1765-1789.

12. Wilbur, M. L., Yeager, W. T., Jr., Wilkie, W. K., Cesnik, C. E. S., and Shin, S. J., "Hover Testing of the NASA/Army/MIT Active Twist Rotor Prototype Blade," American Helicopter Society 56th Annual Forum, Virginia Beach, VA, May 2000.

13. Cesnik, C. E. S., Shin, S. J., and Wilbur, M. L., "Dynamic Response of Active Twist Rotor Blades," Smart Materials and Structrues – Special Issue on Rotorcraft Application, Vol.10, 2001, pp.62-76.

14. Wilbur, M. L., Mirick, P. H., Yeager, W. T., Jr., Langston, C. W., Cesnik, C. E. S., and Shin, S. J., "Vibratory Loads Reduction Testing of the NASA/Army/MIT Active Twist Rotor," Journal of the American Helicopter Society, Vol.47, (2), 2002, pp. 123-133.

15. Wilbur, M. L., Yeager, W. T., Jr., and Sekula, M. K., "Further Examination of the Vibratory Loads Reduction Results from the NASA/Army/MIT Active Twist Rotor Test," American Helicopter Society 58th Annual Forum, Montreal, Canada, June 2002.

16. Bernhard, A. P. F., and Chopra, I., "Hover Test of a Mach-Scale Rotor Model with Active Blade Tips," Journal of the American Helicopter Society, Vol.47, (4), 2002, pp. 273-284.

17. Wereley, N. M., and Hall, S. R., "Linear Time Periodic Systems: Transfer Functions, Poles, Transmission Zeros and Directional Properties," 1991 American Control Conference, Boston, MA, June 1991.

18. Nitzsche, F., "Laplace-Domain Approximation to the Transfer Functions of a Rotor Blade in Forward Flight," Aeronautical Journal, Vol. 105, (1077), 2001, pp. 233-240.

19. Siddiqi, A., and Hall, S. R., "Identification of the Harmonic Transfer Functions of a Helicopter Rotor," AMSL Report #01-01, Active Materials and Structures Laboratory, Massachusetts Institute of Technology, March 2001.

20. Wilkie, W. K., Wilbur, M. L., Mirick, P. H., Cesnik, C. E. S., and Shin, S. J., "Aeroelastic Analysis of the NASA/Army/MIT Active Twist Rotor," American Helicopter Society 55th Annual Forum, Montreal, Canada, May 25-27, 1999.

21. Hall, S. R., and Wereley, N. M., "Performance of Higher Harmonic Control Algorithms for Helicopter Vibration Reduction," Journal of Guidance, Control, and Dynamics, Vol.16, (4), 1993, pp.793-797.

22. Anonymous, ControlDesk Experiment Guide, dSPACE GmbH, Germany, 2001